RSC Advances

PAPER

View Article Online
View Journal | View Issue

Cite this: *RSC Adv.*, 2022, **12**, 12590

Facile preparation of flexible binder-free graphene electrodes for high-performance supercapacitors†

Shiqi Lin, [ab] Jie Tang, *[ab] Wanli Zhang,[ab] Kun Zhang, [a] Youhu Chen, [a] Runsheng Gao,[a] Hang Yin, [ab] Xiaoliang Yu[a] and Lu-Chang Qin [c]

A facile two-step strategy to prepare flexible graphene electrodes has been developed for supercapacitors using thermal reduction of graphene oxide (GO) and thermally reduced graphene oxide (TRGO) composite films. The tunable porous structure of the GO/TRGO film provided channels to release the high pressure generated by CO_2 gas. The graphene electrode obtained from reduced-GO/TRGO (1 : 1 in mass ratio) film showed great flexibility and high film density (0.52 g cm^{-3}). Using the EMI-BF_4 electrolyte with a working voltage of 3.7 V, the as-fabricated free-standing reduced-GO/TRGO (1 : 1) film achieved a great gravimetric capacitance of 180 F g^{-1} (delivering a gravimetric energy density of 85.6 W h kg^{-1}), a volumetric capacitance of 94 F cm^{-3} (delivering a volumetric energy density of 44.7 W h L^{-1}), and a 92% retention after 10 000 charge/discharge cycles. In addition, the solid state flexible supercapacitor with the free-standing reduced-GO/TRGO (1 : 1) film as the electrodes and the EMI-BF_4/poly (vinylidene fluoride hexafluopropylene) (PVDF-HFP) gel as the electrolyte also demonstrated a high gravimetric capacitance of 146 F g^{-1} with excellent mechanical flexibility, bending stability, and electrochemical stability. The strategy developed in this study provides great potentials for the synthesis of flexible graphene electrodes for supercapacitors.

Received 14th March 2022
Accepted 14th April 2022

DOI: 10.1039/d2ra01658c

rsc.li/rsc-advances

1. Introduction

With the rapid development of portable electronic devices in modern society, the growing requirement for flexible electronic technology is becoming more and more urgent.[1–6] One of the greatest challenges in the development of flexible electronic technology is the fabrication of compatible light, thin, and flexible electrochemical energy storage devices. Supercapacitors (SCs), as an important kind of energy storage device, have been applied widely in various applications with excellent power density, faster charging speed, and long cycling-life.[7–13] Many studies have been reported on materials with zero-dimensional (0D), one-dimensional (1D), two-dimensional (2D), and three-dimensional (3D) structures for supercapacitors with improved electrochemical performance.[14–19] Graphene, a 2D nanomaterial, has attracted great attention for fabricating flexible electrodes for SCs because of its large specific surface area, high mechanical strength, and unique layered structure.[20–23] To date, several laboratory methods for fabricating graphene-based flexible electrodes for SCs have been reported. The commonly employed approach has been to design composite structures with polymers,[24,25] carbon nanotubes (CNTs),[26,27] and/or other 2D nanomaterials.[28,29] However, the use of polymers or metal oxides often suffers from short cycling-life, slow frequency response, and poor rate behaviour.[29] In addition, the synthesis process has always involved complicated chemical processes or expensive raw materials, either of which is not advantageous for scalable production. Therefore, it is demanding to develop a facile and efficient way to produce flexible graphene electrode with high mechanical strength, high power density, long cycle life, good flexibility, and improved energy density.

Thermal reduction has been one of the most effective ways to remove the oxygen-containing functional groups from graphene oxide (GO) within seconds and the thus-obtained graphene is named as thermally reduced graphene oxide (TRGO) in this study.[30,31] However, this rapid thermal reduction method is still quite challenging to producing free-standing graphene films directly since quick heating may break the film structure when reduction is applied to the GO film.[31] This is because, on the one hand, the large amount of oxygen-containing groups' decomposition would generate a huge amount of gases such as CO_2,[30,32,33] which would produce great gaseous pressure inside the film. On the other hand, the interactions of hydrogen bonds between the oxygen-containing functional groups would make the GO film very compact without the capability to releasing the pressure and large amount of gases generated in the reduction

[a]*National Institute for Materials Science, 1-2-1 Sengen, Tsukuba, Ibaraki 305-0047, Japan. E-mail: tang.jie@nims.go.jp*

[b]*University of Tsukuba, 1-1-1 Tennodai, Tsukuba, Ibaraki 305-0006, Japan*

[c]*Department of Physics and Astronomy, University of North Carolina at Chapel Hill, Chapel Hill, NC 27599-3255, USA*

† Electronic supplementary information (ESI) available. See https://doi.org/10.1039/d2ra01658c

process.[34] To address this issue, various strategies have been attempted to obtain flexible graphene films. For instance, Vallés *et al.* reported a flexible conductive graphene paper obtained by direct and gentle annealing of GO paper.[35] Wang *et al.* achieved 3D spatial engineering of all-in-one supercapacitors with various architectures in one GO film.[36] Chen *et al.* used a delicately designed apparatus to obtain thermally expanded GO films with controllable and uniform thickness.[37]

In this work, we report a facile two-step thermal reduction of GO to produce free-standing reduced-GO/TRGO films with high flexibility and excellent capacitive behaviour for supercapacitors with both ionic liquid electrolyte and solid state electrolyte. The porous TRGO is introduced into GO to form a GO/TRGO composite film with a tunable porous structure and followed by rapid thermal treatment to realize the reduction of GO components.[33] This method improved the flexibility of the electrode film, which is attributed to the decreased GO content leading to decreasing of generated gases and a porous structure providing channels to release them. The advantages of the proposed approach are multi-folds: (i) no other additives are required such as polymers and/or non-electrochemical active materials; (ii) the mass density of free-standing graphene film can be controlled by tuning the composition ratio of the GO/TRGO film; (iii) the free-standing reduced-GO/TRGO (1 : 1) film has a high gravimetric capacitance of 180 F g^{-1} (delivering a gravimetric energy density of 85.6 W h kg^{-1}) and a volumetric capacitance of 94 F cm^{-3} (delivering a volumetric energy density of 44.7 W h L^{-1}) with an ionic liquid electrolyte (EMI-BF_4); (iv) the solid state flexible supercapacitor with the free-standing reduced-GO/TRGO (1 : 1) film as the electrode and the EMI-BF_4/poly (vinylidene fluoride hexafluopropylene) (PVDF-HFP) gel as the electrolyte also shows a high gravimetric capacitance of 146 F g^{-1} with a good mechanical flexibility, bending stability, and excellent electrochemical stability. Therefore, the free-standing reduced-GO/TRGO graphene-based electrodes fabricated by this approach are a competitive candidate for high performance supercapacitors.

2. Experimental

2.1. Preparation of free-standing graphene film

GO was obtained from graphite using the Hummers' method.[38] The aqueous GO suspension with a concentration of 1 g L^{-1} was first dried in a freeze drier for two days. The obtained sponge-like GO was then heat-treated at 500 °C to obtain TRGO. The GO/TRGO composite films with different weight ratios of GO/TRGO (1 : 0, 3 : 1, 1 : 1, 1 : 3, 0 : 1) were fabricated by vacuum filtration of the corresponding mixture of GO and TRGO dispersions in ethanol with a concentration of 0.5 g L^{-1} onto PTFE filter papers. After drying, free-standing GO/TRGO films were obtained by peeling from filter papers. The free-standing GO/TRGO films were then thermally treated at 500 °C again to reduce the GO and produce the reduced-GO/TRGO films for use as supercapacitor electrodes. The TRGO electrode was also synthesized by directly filtering the TRGO dispersion on PTFE filter paper and drying in a vacuum oven.

2.2. Microstructure characterization

The morphologies of the obtained GO/TRGO and reduced-GO/TRGO films were characterized by field-emission scanning electron microscopy (SEM, JSM-6500F, JEOL) and transmission electron microscopy (TEM, JEM-2100, JEOL). The crystalline phases of these films were examined by powder X-ray diffraction (XRD, Rigaku SmartLab using Cu-K_α radiation with wavelength $\lambda = 1.5418$ Å) in the 2θ range of 5°–60°. Raman spectroscopy ($\lambda =$ 532 nm, Nanophoton Raman Plus) and Fourier transform infrared spectroscopy (FTIR, JASCO FT/IR-6100) were also employed to characterize the structural features. The specific surface area and distribution of pores were measured by the nitrogen adsorption–desorption method (Quantachrome autosorb iQ). Surface chemistry of materials was characterized by X-ray photoelectron spectroscopy (XPS, ULVAC-PHI Quantera SXM) with a twin anode Al K_α X-ray source and hemispherical energy analyser. The absorption energies were calibrated against the aliphatic carbon C 1s peak at 284.5 eV.

2.3. Electrochemical measurement

To evaluate the electrochemical performance of the fabricated graphene film, coin cells were assembled directly using the free-standing graphene film of a diameter of 15 mm as the electrodes with a layer of glass fibre membrane as the separator. To demonstrate the application of the free-standing films in flexible supercapacitors, a solid state supercapacitor was also fabricated. The gel electrolyte was prepared by a solution-cast method.[39,40] Typically, 0.5 g PVDF-HFP and 2 g EMI-BF_4 were added to 20 mL acetone at 60 °C with vigorous stirring for 2 hours. Then, the obtained solution was cast into a Petri dish and the acetone was completely evaporated by vacuum drying at 60 °C for 12 hours. Finally, the EMI-BF_4/PVDF-HFP gel electrolyte was obtained with a thickness of about 250 μm. To fabricate a flexible solid state supercapacitor, two pieces of free-standing reduced-GO/TRGO films (2.5 cm × 2.0 cm) with a 5 mm wide aluminum external terminal and a piece of EMI-BF_4/PVDF-HFP gel electrolyte (2.7 cm × 2.2 cm) were assembled in a sandwich structure. The resulting assembly was then encapsulated in a three-side-sealed PET pouch. Finally, the remaining side was vacuum-sealed to obtain the flexible solid state supercapacitor. It should be pointed out that, in order to avoid the influence of moisture in the air, all operations were carried out in an Ar-filled glove box.

The electrochemical properties and capacitance of the supercapacitors were evaluated in a two-electrode system by cyclic voltammetry (CV), galvanostatic charge–discharge curves (GCC), and electrochemical impedance spectroscopy (EIS) using an electrochemical workstation (Biologic VSP-300). The CV response of the electrodes was measured at different scan rates varying from 10 to 100 mV s^{-1}. The CV and GCC tests of supercapacitors in ionic liquid electrolytes were performed in the range from 0 to 3.7 V. EIS measurements were carried out (without DC bias sinusoidal signal of 0.005 V) over the frequency range from 10 kHz to 0.1 Hz. The cyclic performance measurements were conducted with a charge–discharge current density of 1 A g^{-1} using a Land Battery Test System.

Based on the results of the GCC tests, the gravimetric specific capacitance was calculated from the discharging time at every current density by using the following equation[41]

$$C_m = \frac{4I \times t}{U \times m} \quad (1)$$

where C_m is the gravimetric specific capacitance of the supercapacitor, I/m is the applied current density, t is the time for discharging, and U is the potential window. The volumetric specific capacitance was calculated from the gravimetric specific capacitance based on the following equation[42,43]

$$C_V = C_m \times \rho \quad (2)$$

where C_V is the volumetric specific capacitance of the supercapacitor, C_m is the gravimetric specific capacitance of the supercapacitor, and ρ is the bulk density of the electrode.

3. Results and discussion

3.1. Preparation of flexible graphene films

Fig. 1 illustrates schematically the synthesis of flexible graphene electrode by thermal reduction of the GO/TRGO composite film. The GO/TRGO dispersion was prepared by mixing the dispersions of GO and TRGO at a ratio of 1 : 1. It was found that the GO/TRGO dispersion was stable without precipitation even after 1 week's storage. Although the TRGO dispersion showed good dispersibility after sonication, it settled out completely after 1 week. This suggests that GO and TRGO formed a composite through the π–π stacking interactions in the solution, thereby improving the dispersion stability of TRGO. With the vacuum-assisted assembly and π–π stacking interactions between the GO and TRGO sheets,[44] a laminated film with alternating GO and TRGO structure, as illustrated in Fig. 1, was obtained. Fig. 2a and b show the cross-sectional SEM images of the GO and GO/TRGO (1 : 1) films, respectively. The GO film had a laminated compact structure as a result of hydrogen bonding interactions between the oxygen-containing functional groups on the GO sheet.[45] While the GO/TRGO film exhibited a lot of porous structures, the difference in the structure of the GO/TRGO film and GO film suggested that the addition of TRGO hindered the formation of hydrogen bonds between the GO sheets (illustrated in Fig. S1†) and was beneficial to the formation of a more porous film. An analysis of the film density showed that the densities of the GO film and the GO/TRGO film were 1.01 g cm^{-3} and 0.77 g cm^{-3}, respectively, which is consistent with SEM observations.

The GO in these prepared composite films was then reduced to graphene by thermal annealing. As shown in the photographs in Fig. 1, the reduced-GO/TRGO film obtained with thermal annealing of the GO/TRGO precursor retained its morphology and gained additional flexibility. Cross-sectional SEM analyses (Fig. 2c) showed that the uniform structure was still maintained after thermal annealing, though a slight increase in thickness (from 33 μm to 41 μm) was observed. As revealed in Fig. 2b and c, more porous interlayer structures were introduced into the reduced-GO/TRGO film, which were due to the fact that flat GO sheets became wrinkled TRGO sheets after reduction and resulting in a decrease in the film density from 0.77 g cm^{-3} to 0.52 g cm^{-3}. To further characterize the mechanical strength of the free-standing film, the electrode was bent to an 'arch like' structure to evaluate its flexibility. The bending angle was nearly 180° with a radius of curvature as small as 1.28 mm (Fig. 2d) without fracture. It demonstrates that the reduced-GO/TRGO film has a good mechanical flexibility. In contrast, after thermal annealing, the GO film was broken into pieces with a loose structure (Fig. S2†) due to the inability to eliminate rapidly the gases generated during the reduction process. These results indicate that the introduction of TRGO was crucial to the successful fabrication of free-standing flexible graphene films. On the one hand, it can reduce the gases generated during the reduction process. On the other hand, the porous structure produced by hindering the formation of hydrogen bonds between the GO sheets can provide enough channels to eliminate rapidly the gases generated during the reduction process to obtain an intact graphene film.

The morphology and structure of the GO/TRGO composite film and the reduced-GO/TRGO film were further characterized by transmission electron microscopy (TEM). Fig. 3a is a low-magnification TEM image showing the morphology of the GO/TRGO composite. The high-resolution TEM (HRTEM) image (Fig. 3b) reveals the composited microstructure of TRGO and GO nanosheets. Since the TRGO nanosheets were crystalline while the GO nanosheets were amorphous, the power spectra of the selected areas revealed both crystalline domains due to TRGO (inset i) and amorphous regions due to GO (inset ii). The d-spacing of 0.23 nm corresponds to the (100) lattice planes of graphite. Fig. 3c shows a typical overview of the reduced-GO/TRGO composite film, where folded graphene was observed clearly. The HRTEM image (Fig. 3d) revealed that the reduced-GO/TRGO nanosheets had fine crystallinity after rapid thermal reduction.

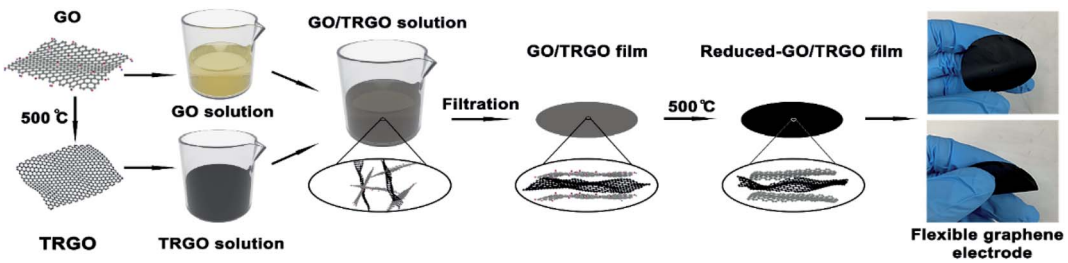

Fig. 1 Schematic illustration of synthesis process of flexible free-standing reduced-GO/TRGO film.

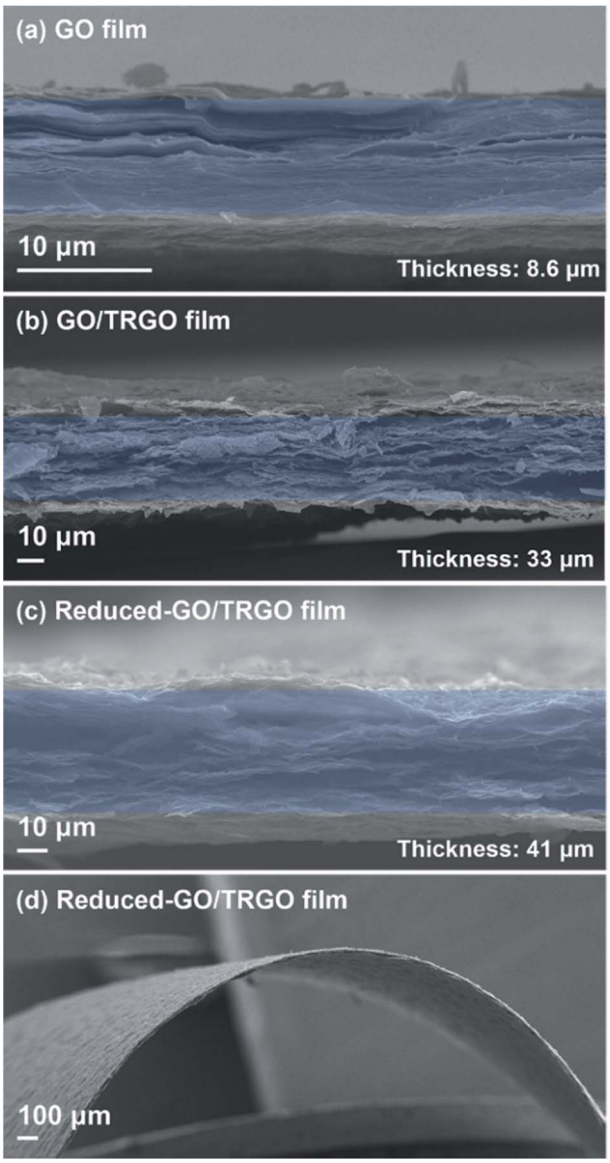

Fig. 2 Cross-sectional SEM images of (a) GO film; (b) GO/TRGO (1 : 1) film; (c) reduced-GO/TRGO (1 : 1) film, and (d) bent reduced-GO/TRGO (1 : 1) film with radius of curvature of 1.28 mm.

3.2. Analysis of flexible graphene films

As shown in Fig. 4, the crystalline structure of the GO film, the GO/TRGO film, and the reduced-GO/TRGO film were characterized by X-ray diffraction. The first sharp peak from the GO film was at $2\theta = 12.2^{\circ}$, corresponding to a separation of 0.73 nm between the GO sheets.[46] After introducing the TRGO sheets, the diffraction peak became broader and shifted to $2\theta = 11.0^{\circ}$ (corresponding to a d-spacing of 0.80 nm), indicating the addition of TRGO prevented GO sheets from restacking and led to the formation of a loose structure. In the meanwhile, the appearance of a very weak peak at $2\theta = 24.8^{\circ}$ is attributed to the formation of graphitic microcrystals on the graphene plane.[47] After the thermal treatment, the peak at $2\theta \approx 10^{\circ}$ disappeared and a broad peak at $2\theta = 24.3^{\circ}$ emerged, which suggests the

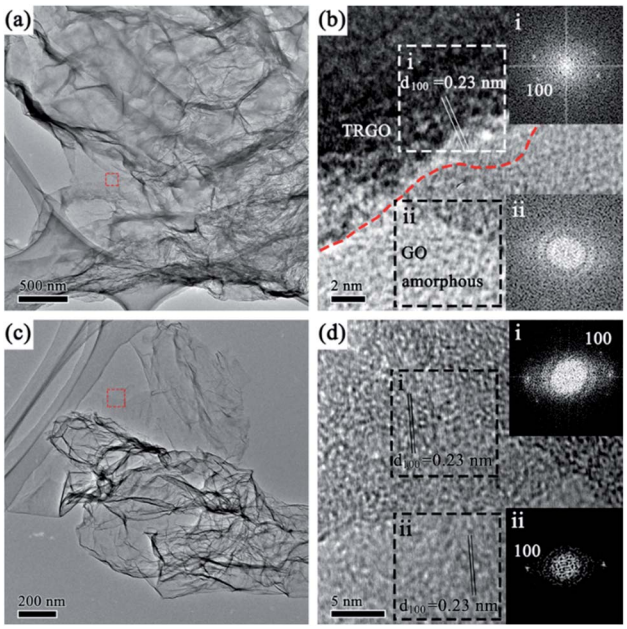

Fig. 3 TEM images of GO/TRGO composite film and reduced-GO/TRGO film. (a) Low magnification TEM image showing an overview of GO/TRGO nanosheets. (b) HRTEM image of GO/TRGO nanosheets marked in (a), with d-spacing of 0.23 nm corresponding to (100) of graphite. The crystalline domain is due to TRGO and the amorphous region pertains to GO. (c) Low magnification TEM image showing an overview of reduced-GO/TRGO film. (d) HRTEM image of reduced-GO/TRGO film showing clear crystallinity in graphene after rapid thermal reduction.

formation of more graphitic microcrystals due to the reduction of GO. The resulting film becomes disordered due to the impact of the gases generated in the reduction reactions.

Raman spectra of the GO film, GO/TRGO film, and reduced-GO/TRGO film are presented in Fig. 5. The samples showed the typical D peak and G peak around 1360 and 1580 cm^{-1},

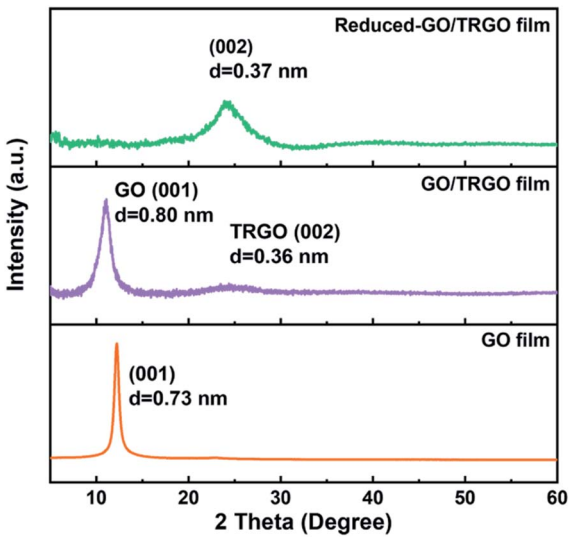

Fig. 4 XRD patterns of GO, GO/TRGO, and reduced-GO/TRGO films.

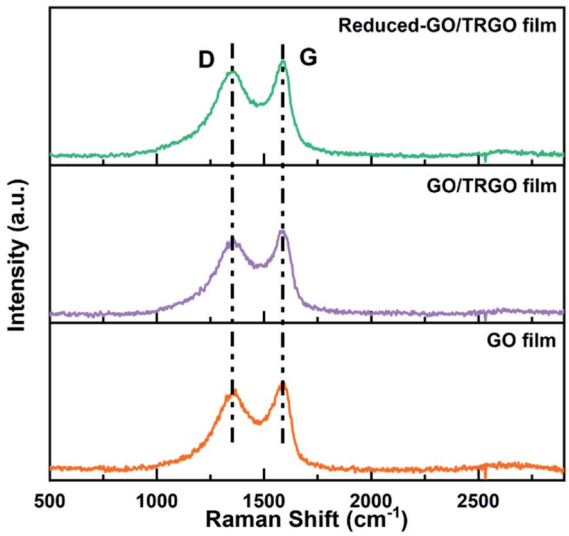

Fig. 5 Raman spectra of GO, GO/TRGO, and reduced-GO/TRGO films.

respectively, fitted with a Gaussian profile. The D peak in carbon materials is attributed to the structural defects and disordered sp^2 bonded carbon. Therefore, the intensity ratio of the fitted D peak and G peak (I_D/I_G) was calculated to measure the concentration of structural defects in the samples as shown in Table S1.† The I_D/I_G ratio for GO film is 0.93 and it increased to 0.96 for the GO/TRGO film. This is because TRGO has a larger I_D/I_G ratio of 0.97 (Fig. S3†). After thermal treatment, the obtained reduced-GO/TRGO film showed an I_D/I_G ratio of 0.98, indicating the introduction of more defects accompanied by removal of the functional groups in the reduction process.

To monitor the chemical composition of the obtained films at different steps, XPS measurements were carried out. As shown in Fig. 6a, the pure GO film showed a strong O 1s peak with an oxygen content of 29.3%, corresponding to an atomic C/O ratio of 2.3. The fitting of the C 1s peak (Fig. 6b) reveals that the GO film has a large number of C–OH, C–O–R, and C=O functional groups, whereas the GO/TRGO film (Fig. 6a) showed a relatively low oxygen content of 22.0% with a C/O ratio of 3.5 due to the introduction of TRGO with an oxygen content of 16.2% and a C/O ratio of 5.2 (Fig. S4†). It is worth noting that the C/O ratio of the GO/TRGO film (3.5) is very close to the calculated C/O ratio (3.7) according to ratio of mixing of GO and TRGO (1 : 1), suggesting a fairly homogeneous distribution of GO and TRGO in the composite film. After the thermal treatment, the C/O ratio was further increased to 5.8 in the obtained reduced-GO/TRGO film. Correspondingly, as shown in Fig. 6b, the relative peak intensity of oxygen-containing C–OH, C–O–R, and C=O functional groups was reduced significantly, suggesting that the GO component in the GO/TRGO film had been reduced to graphene. The films were also examined with FT-IR spectroscopy as shown in Fig. S5.† From the FT-IR spectra, the GO film contained abundant oxygenic groups. It showed apparent peaks at 3420 cm^{-1}, 1722 cm^{-1}, 1611 cm^{-1}, 1044 cm^{-1}, and 960 cm^{-1}, corresponding to the vibrations of –OH, C=O, C=C, and C–O groups, respectively.[48,49] These characteristic peaks remained apparent in the GO/TRGO film with a relatively low intensity. After the thermal treatment, however, the obtained reduced-GO/TRGO film only showed weak C=O and C=C peaks, suggesting successful reduction of GO in the GO/TRGO film. These FTIR results are consistent and in good agreement with the XPS analysis.

To obtain a quantitative picture of the evolution of the porous structure of the electrode films with different compositions, the nitrogen adsorption and desorption isotherms were measured as shown in Fig. 7a. The pore size distributions of these films were analyzed by the DFT method as shown in Fig. 7b. The pure GO film possessed few pores with diameter less than 2 nm and had a specific surface area (SSA) of 8.9 m^2 g^{-1}. This is consistent with its cross-sectional SEM image displayed in Fig. 2a, showing a compact film with a density of

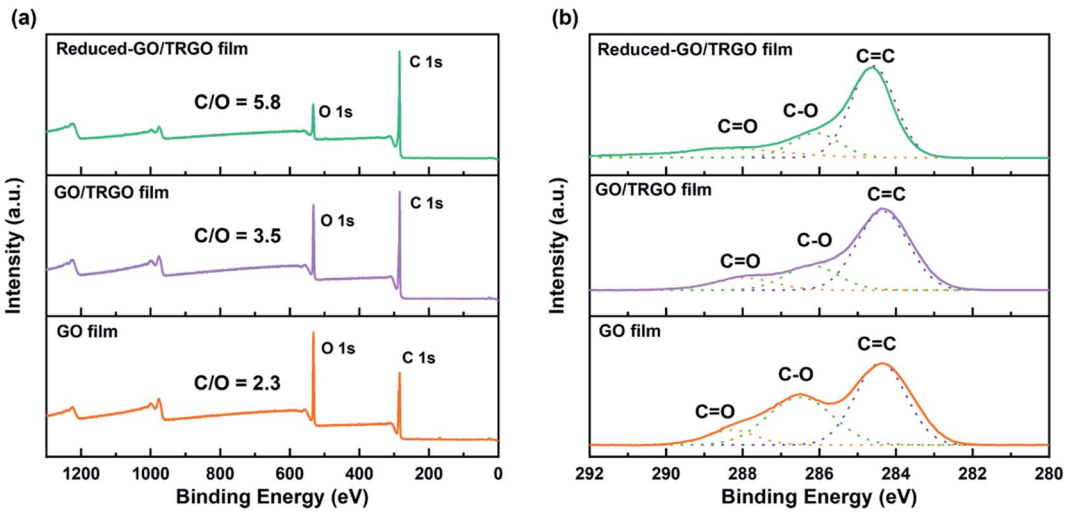

Fig. 6 (a) XPS survey spectra of GO, GO/TRGO, and reduced-GO/TRGO films. (b) XPS high-resolution C 1s spectra of GO, GO/TRGO, and reduced-GO/TRGO films.

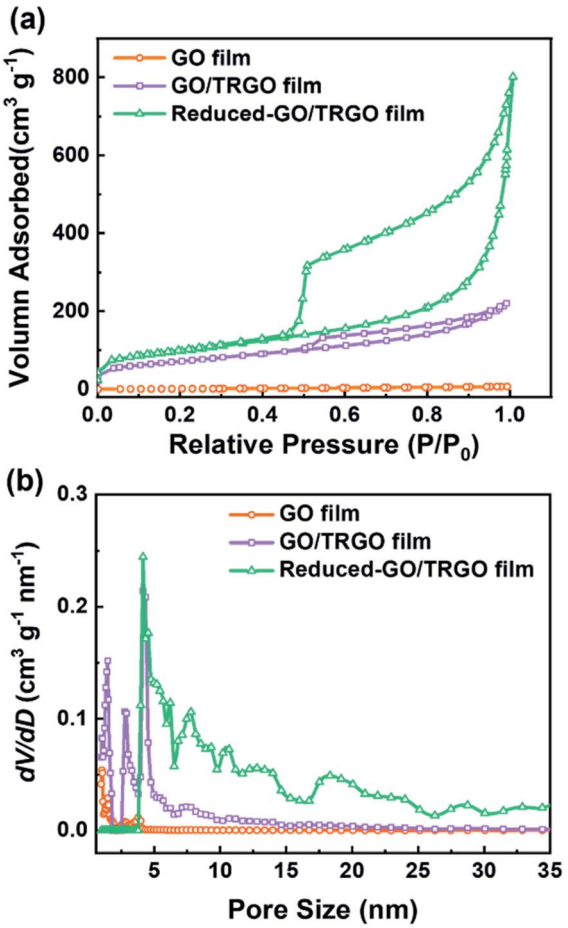

Fig. 7 (a) Nitrogen adsorption/desorption isotherms and (b) pore size distribution of GO, GO/TRGO, and reduced-GO/TRGO films.

1.01 g cm^{-3}. These features are attributed to the strong hydrogen bonds between the functional groups. The GO/TRGO (1 : 1) film showed a typical type IV adsorption/desorption isotherm with a type H4 hysteresis loop, indicating the presence of nonrigid slit-shaped pore-structures. The SSA of GO/TRGO (1 : 1) film increased to 218 m^2 g^{-1} and was accompanied by an increase in both pore size and pore volume. It should be emphasized that the pore structure of the obtained film is related to the ratio of GO and TRGO. According to the results summarized in Table S2,† the SSA of the obtained film increased with increasing portion of TRGO in the film. Correspondingly, as shown in Fig. S6,† both the pore size and pore volume of these films also increased. This result suggests that the ratio of GO/TRGO played an important role in the pore structure of the film, because the compact stacking of GO sheets could be inhibited by the presence of TRGO sheets.

After thermal reduction, the obtained reduced-GO/TRGO (1 : 1) film displayed a similar type IV adsorption/desorption isotherm (Fig. 7a), while the nitrogen adsorption increased with the relative pressure (P/P_0) over 0.9, indicating the production of more pores during the reduction process. The SSA of the reduced-GO/TRGO (1 : 1) film further increased to 290 m^2 g^{-1} and was accompanied by a decreasing film density of 0.52 g cm^{-3}. The pore distribution calculated by the DFT method, shown in Fig. 7b, revealed that the reduced-GO/TRGO film had more micropores with size ranging from 4 to 25 nm. After thermal reduction, the increase in the microporosity of the reduced-GO/TRGO film was contributed, on the one hand, by changes of the morphology from planar GO sheets to wrinkled TRGO sheets during the GO reduction process. On the other hand, the reduction of GO was accompanied by the removal of oxygen-containing functional groups, which inhibited the formation of hydrogen bonds and weakened the interactions between the produced TRGO sheets, making it easier to form a porous structure with a greater SSA.

3.3. Capacitive performance of free-standing graphene film in supercapacitors

To evaluate the electrochemical properties of the free-standing reduced-GO/TRGO (1 : 1) film, symmetric supercapacitors were fabricated using EMI-BF_4 as the electrolyte. For comparison, the filtered TRGO films were also prepared and used as the electrodes for supercapacitors with EMI-BF_4 as the electrolyte. Fig. 8a shows the CV curves for supercapacitors with the free-standing reduced-GO/TRGO (1 : 1) film and the filtered TRGO film electrodes at low and fast voltage sweep rate, respectively. It can be seen clearly that both CV curves exhibited rectangular shapes without any redox reaction peaks at the low scanning rate of 10 mV s^{-1}, suggesting an ideal capacitive behaviour.[29,50] With an increase of the scanning rate to 100 mV s^{-1}, the CV curve for the free-standing reduced-GO/TRGO (1 : 1) film still retained a nearly rectangular loop, implying a superior rate stability. However, the CV curve of filtered TRGO film exhibited an obvious deviation from the rectangular shape when the scan speed reached 100 mV s^{-1}. As shown in Fig. S7,† this trend was observed more pronounced at the higher scanning rate of 200 mV s^{-1}. This result implied that the free-standing reduced-GO/TRGO (1 : 1) film had a better rate capability. It should be pointed out that the same trend was also observed in the galvanostatic charge–discharge measurements. As shown in Fig. 8b, at a low charge–discharge current density of 0.2 A g^{-1}, the charge–discharge curves of both electrodes exhibited ideal isosceles triangular shape, indicating an excellent capacitive behavior.[51] The gravimetric specific capacitances of the free-standing reduced-GO/TRGO (1 : 1) film and the filtered TRGO film were 180 F g^{-1} (delivering a gravimetric energy density of 85.6 W h kg^{-1}) and 193 F g^{-1} (delivering a gravimetric energy density of 91.7 W h kg^{-1}), respectively. This result is superior to other reported graphene-based electrochemical capacitors as shown in Table S3.†[26,52–59] The charge–discharge curves of both electrodes at different current densities from 0.2 to 10 A g^{-1} are shown in Fig. S8.† When the current density was increased from 0.2 to 10 A g^{-1}, the gravimetric specific capacitance of the filtered TRGO film exhibited a large decrease from 193 F g^{-1} to 108 F g^{-1}, and the capacity retention was only 56%, as shown in Fig. 8c. However, the gravimetric specific capacitance of the free-standing reduced-GO/TRGO (1 : 1) film showed only a slight decrease, from 180 F g^{-1} to 139 F g^{-1}, corresponding to a higher capacity retention rate of 77%, which proved that the

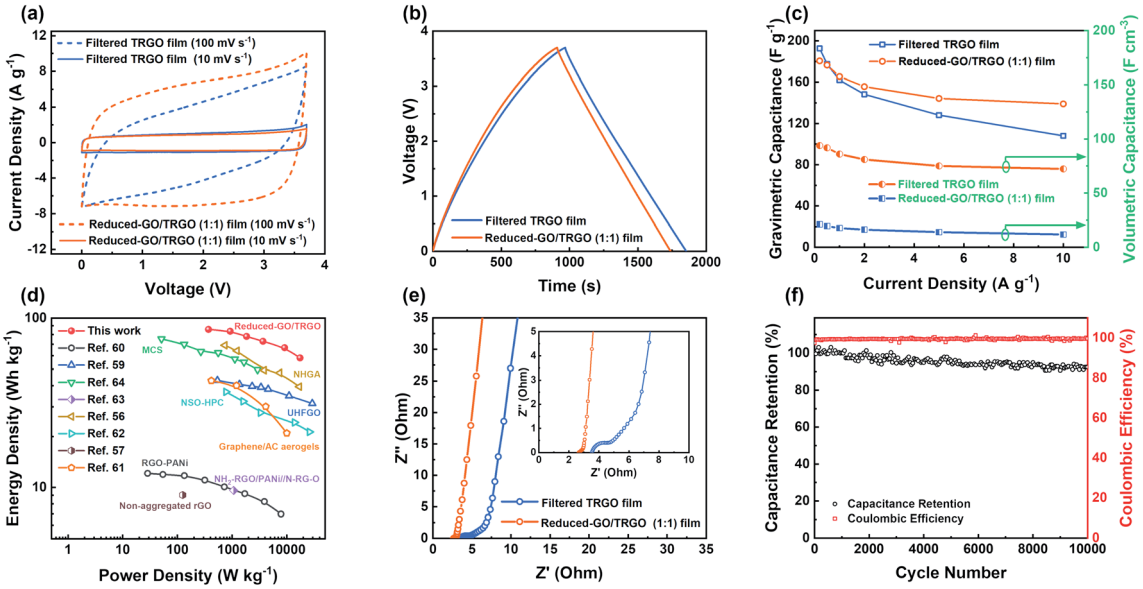

Fig. 8 (a) CV curves at slow voltage sweep rate of 10 and 100 mV s^{-1}. (b) Charge and discharge curves at constant current density of 0.2 A g^{-1}. (c) Gravimetric and volumetric specific capacitance at various current densities from 0.2 to 10 A g^{-1}. (d) Ragone plots of supercapacitor with free-standing reduced-GO/TRGO (1 : 1) film and comparison with devices using other 2D materials reported in literature. (e) Nyquist plots of supercapacitors with free-standing reduced-GO/TRGO (1 : 1) film and filtered TRGO film electrodes, respectively. (f) Cycling stability of supercapacitor with free-standing reduced-GO/TRGO (1 : 1) film.

free-standing film had an excellent rate capability. It is consistent with the CV measurements. Additionally, the Ragone plots derived from the discharge curves are shown in Fig. 8d. The free-standing reduced-GO/TRGO (1 : 1) film electrode exhibited an energy density of 85.6 W h kg^{-1} with a corresponding power density of 0.37 kW kg^{-1}. Even at a high power density of 17.4 kW kg^{-1}, the free-standing reduced-GO/TRGO (1 : 1) film electrode still delivered a high energy density of 58.1 W h kg^{-1}. It is superior to other reported graphene-based electrode materials.[33,56,59–65]

To explain the markedly different electrochemical behaviours exhibited by the two films, we further investigated the difference in the pore structures between the free-standing reduced-GO/TRGO (1 : 1) film and the filtered TRGO film. According to the results of SEM (Fig. S9†) and BET (Fig. S10†) analysis, the filtered TRGO film had a greater specific surface area, larger pore size, and lower film density of 0.11 g cm^{-3}. Therefore, we attribute the slightly higher gravimetric specific capacitance of the filtered TRGO film to its greater specific surface area and the loose structure. However, the volumetric specific capacitances of these two films (a more important factor to consider in some applications of supercapacitors) are vastly different. By considering the density of the electrode films, as shown in Fig. 8c, the volumetric specific capacitance of free-standing reduced-GO/TRGO (1 : 1) film (94 F cm^{-3}) is significantly greater than that of the filtered TRGO film (21 F cm^{-3}) at a current density of 0.2 A g^{-1}. The supercapacitor with free-standing reduced-GO/TRGO (1 : 1) electrodes exhibited a very high volumetric energy density of 44.7 W h L^{-1}, which is almost 5 times of the commercial supercapacitors (5–8 W h L^{-1}).[43,62,66–70] Compared to the filtered TRGO film, the free-standing reduced-GO/TRGO (1 : 1) film has a density nearly a 4.5 times increase in volumetric specific capacitance in spite of 7% lower in gravimetric specific capacitance. This shows that our method for preparing flexible films can maximize the retention of the microporous structure required for charge storage and ion diffusion while increasing the density of the film, thereby enhancing the mechanical strength of the film. In addition, the increase of film density would also enhance the contact between graphene sheets and reduce the resistance between graphene sheets, thereby improving the conductivity of the electrode film. This was confirmed by subsequent EIS analysis.

Fig. 8e shows the Nyquist plots for the supercapacitors with free-standing reduced-GO/TRGO (1 : 1) films and the filtered TRGO films, respectively. Both plots have almost vertical curves in the low-frequency region, indicating an apparent capacitive behavior. As expected, the equivalent series resistance (R_S) estimated from the intercept on the x-axis for the free-standing reduced-GO/TRGO (1 : 1) film (2.7 Ω) is lower than that of the filtered TRGO film (3.6 Ω), which is ascribed to improvement in the conductivity of the former due to promotion of charge transport in the film by enhancement of the contact between the graphene sheets. The inset in the figure shows that the supercapacitor with the filtered TRGO film had a small semicircle (corresponding to the charge transfer resistance R_{ct}) and a 45° straight line (corresponding to the electrolyte diffusion in the electrode) in the high-frequency region and the intermediate-frequency region. However, no noticeable semicircle was observed in the high frequency region, and the 45° Warburg line was also significantly shortened, which indicated that the free-standing reduced-GO/TRGO (1 : 1) film had a lower

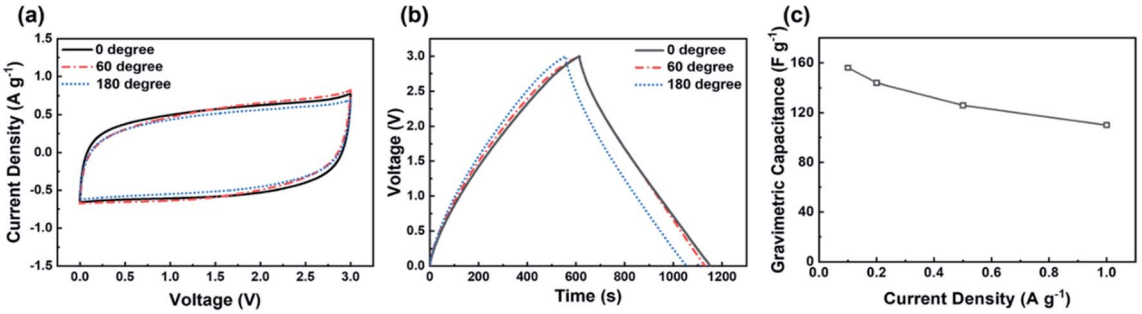

Fig. 9 (a) Cyclic voltammetry curves and (b) charge and discharge curves of flexible solid state supercapacitor at different bending angles. (c) Gravimetric specific capacitance of flexible solid state supercapacitor at various current densities from 0.1 to 1.0 A g^{-1}.

charge transfer resistance and electrolyte diffusion resistance due to a large number of mesopores in the electrode film (Fig. 7b), facilitating fast mass transport of electrolyte.[71–74] It suggests that the prepared free-standing film facilitated the electrolyte ions to diffuse more easily within the film and also reduced the electrode/electrolyte interface resistance. In addition, the cyclic testing of supercapacitor with the free-standing reduced-GO/TRGO (1 : 1) film electrodes at a current density of 1 A g^{-1} was carried out. It confirmed that the supercapacitor had an excellent cycling stability with a high average coulombic efficiency of 99% during the cycling test and 92% retention of its initial specific capacitance after 10 000 cycles (Fig. 8f).

In order to demonstrate the application of the prepared free-standing films in flexible supercapacitors, we assembled a flexible solid state supercapacitor with the free-standing reduced-GO/TRGO (1 : 1) film as the electrodes, EMI-BF_4/poly(-vinylidene fluoride hexafluopropylene) (PVDF-HFP) gel as the electrolyte, and encapsulated them with two pieces of flexible PET films (Fig. S11†). The use of EMI-BF_4/PVDF-HFP gel electrolyte enabled flexible supercapacitors with higher working voltages, which is beneficial for their practical applications. Fig. 9a shows the CV curves of the flexible supercapacitor subjected to different bending angles at a scan rate of 10 mV s^{-1}. It can be seen from the figure that the curves at different bending angles almost overlapped, and the shape of the CV curves almost did not change when the bending angle reached 180°. Fig. 9b shows the charge–discharge curves of the flexible supercapacitor at different bending angles and they all were in an isosceles triangular shape, indicating an excellent capacitive behaviour. When the bending angle was 0°, 60° and 180°, the corresponding gravimetric specific capacitance of the flexible supercapacitor was 146, 143, and 135 F g^{-1}, respectively. When the bending angle increased from 0° to 180°, the capacitance retention was about 92.5% without obvious attenuation. These measurements suggest that the free-standing reduced-GO/TRGO (1 : 1) film based supercapacitor had good mechanical flexibility and excellent electrochemical stability. Furthermore, when the charge and discharge current density was increased from 0.1 to 1.0 A g^{-1} (Fig. 9c), the specific capacitance was decreased from 156 F g^{-1} to 110 F g^{-1}, corresponding to a retention of 70.5%. It reveals that the flexible supercapacitor has also good rate performance. As shown in Fig. S12,† the retention rate of specific capacitance of this supercapacitor was 93% after 200 repeated bending, confirming an excellent mechanical flexibility of the free-standing reduced-GO/TRGO (1 : 1) film. To further demonstrate the operation performance of the free-standing reduced-GO/TRGO (1 : 1) films for supercapacitors, they were used to power an LED light, which showed a stable lighting during the process of bending the flexible supercapacitor (video available in ESI†). The above results strongly suggest that the free-standing reduced-GO/TRGO (1 : 1) film is a promising and suitable candidate as the electrode of flexible supercapacitors.

4. Conclusions

In summary, we have established a facile two-step thermal reduction method to fabricate binder-free and flexible free-standing graphene electrodes for high-performance supercapacitors. It was demonstrated that the formation of a stable GO/TRGO intermediating film with suitable porous structures was the key to the success of this approach. The graphene electrode reduced from GO/TRGO (1 : 1, mass ratio) film showed great flexibility and high film density (0.52 g cm^{-3}). With the EMI-BF_4 electrolyte, the supercapacitor with the free-standing reduced-GO/TRGO (1 : 1) film electrodes showed a high gravimetric and volumetric specific capacitance of 180 F g^{-1} and 94 F cm^{-3}, respectively. It is worth pointing out that its volumetric energy density (44.7 W h L^{-1}) is more than 5 times of commercial supercapacitors (5–8 W h L^{-1}). In addition, the solid state flexible supercapacitor with the free-standing reduced-GO/TRGO (1 : 1) film electrodes and EMI-BF_4/poly (PVDF-HFP) gel electrolyte also showed a high gravimetric specific capacitance of 146 F g^{-1} with a good mechanical flexibility, bending capability, and excellent electrochemical stability. The strategy developed in this study provided great potentials for synthesis of flexible graphene electrodes for supercapacitors.

Author contributions

Shiqi Lin: conceptualization, investigation, formal analysis, visualization, writing – original draft. Jie Tang: conceptualization, formal analysis, writing – review and editing, supervision,

project administration, funding acquisition. Wanli Zhang: investigation, visualization. Kun Zhang: visualization, validation, writing – review and editing. Youhu Chen: visualization. Runsheng Gao: visualization. Hang Yin: visualization. Xiaoliang Yu: visualization. Lu-Chang Qin: visualization, writing – review and editing.

Conflicts of interest

There are no conflicts of interest to declare.

Acknowledgements

A part of this work was supported by NIMS Microstructural Characterization Platform as a program of "Nanotechnology Platform" of the Ministry of Education, Culture, Sports, Science and Technology (MEXT), Japan.

References

1 L. Li, Z. Wu, S. Yuan and X.-B. Zhang, *Energy Environ. Sci.*, 2014, **7**, 2101–2122.
2 X. Wang, X. Lu, B. Liu, D. Chen, Y. Tong and G. Shen, *Adv. Mater.*, 2014, **26**, 4763–4782.
3 V. L. Pushparaj, M. M. Shaijumon, A. Kumar, S. Murugesan, L. Ci, R. Vajtai, R. J. Linhardt, O. Nalamasu and P. M. Ajayan, *Proc. Natl. Acad. Sci. U. S. A.*, 2007, **104**, 13574–13577.
4 D. Gates Byron, *Flexible Electron.*, 2019, **3**, 1–417.
5 L. Dong, C. Xu, Y. Li, Z.-H. Huang, F. Kang, Q.-H. Yang and X. Zhao, *J. Mater. Chem. A*, 2016, **4**, 4659–4685.
6 W.-J. Song, S. Lee, G. Song, H. Bin Son, D.-Y. Han, I. Jeong, Y. Bang and S. Park, *Energy Storage Mater.*, 2020, **30**, 260–286.
7 J. R. Miller and P. Simon, *Science*, 2008, **321**, 651–653.
8 P. Simon and Y. Gogotsi, *Nat. Mater.*, 2008, **7**, 845–854.
9 L. L. Zhang and X. S. Zhao, *Chem. Soc. Rev.*, 2009, **38**, 2520–2531.
10 C. Liu, F. Li, L.-P. Ma and H.-M. Cheng, *Adv. Mater.*, 2010, **22**, 28–62.
11 Y. Wang, Z. Shi, Y. Huang, Y. Ma, C. Wang, M. Chen and Y. Chen, *J. Phys. Chem. C*, 2009, **113**, 13103–13107.
12 Z. Yang, J. Tian, Z. Yin, C. Cui, W. Qian and F. Wei, *Carbon*, 2019, **141**, 467–480.
13 K. Zhang, J. Tang, J. Yuan, J. Li, Y. Sun, Y. Matsuba, D.-M. Zhu and L.-C. Qin, *ACS Appl. Nano Mater.*, 2018, **1**, 2877–2884.
14 P. Chang, H. Mei, Y. Zhao, M. Zhang, X. Wang, L. Cheng and L. Zhang, *Carbon*, 2022, **187**, 375–385.
15 P. Chang, H. Mei, Y. Zhao, W. Huang, S. Zhou and L. Cheng, *Adv. Funct. Mater.*, 2019, **29**, 1–13.
16 P. Chang, H. Mei, M. Zhang, Y. Zhao, X. Wang, L. Cheng and L. Zhang, *Small*, 2021, **17**, 2102639.
17 Q. Ke and J. Wang, *J. Materiomics*, 2016, **2**, 37–54.
18 D. Wang, Y. Xiao, X. Luo, Z. Wu, Y.-J. Wang and B. Fang, *ACS Sustainable Chem. Eng.*, 2017, **5**, 2509–2515.
19 B. Fang, J. H. Kim, M.-S. Kim and J.-S. Yu, *Acc. Chem. Res.*, 2013, **46**, 1397–1406.
20 Y. Shao, M. F. El-Kady, L. J. Wang, Q. Zhang, Y. Li, H. Wang, M. F. Mousavi and R. B. Kaner, *Chem. Soc. Rev.*, 2015, **44**, 3639–3665.
21 L. Huang, D. Santiago, P. Loyselle and L. Dai, *Small*, 2018, **14**, 1800879.
22 M. F. El-Kady, V. Strong, S. Dubin and R. B. Kaner, *Science*, 2012, **335**, 1326–1330.
23 Z. Niu, J. Chen, H. H. Hng, J. Ma and X. Chen, *Adv. Mater.*, 2012, **24**, 4144–4150.
24 K. Chi, Z. Zhang, J. Xi, Y. Huang, F. Xiao, S. Wang and Y. Liu, *ACS Appl. Mater. Interfaces*, 2014, **6**, 16312–16319.
25 J. Zhang, P. Chen, B. H. L. Oh and M. B. Chan-Park, *Nanoscale*, 2013, **5**, 9860–9866.
26 X. Li, Y. Tang, J. Song, W. Yang, M. Wang, C. Zhu, W. Zhao, J. Zheng and Y. Lin, *Carbon*, 2018, **129**, 236–244.
27 S. Yue, H. Tong, L. Lu, W. Tang, W. Bai, F. Jin, Q. Han, J. He, J. Liu and X. Zhang, *J. Mater. Chem. A*, 2017, **5**, 689–698.
28 J. Yan, C. E. Ren, K. Maleski, C. B. Hatter, B. Anasori, P. Urbankowski, A. Sarycheva and Y. Gogotsi, *Adv. Funct. Mater.*, 2017, **27**, 1–10.
29 C. X. Guo and C. M. Li, *Energy Environ. Sci.*, 2011, **4**, 4504–4507.
30 M. J. Mcallister, J.-L. Li, D. H. Adamson, H. C. Schniepp, A. A. Abdala, J. Liu, M. Herrera-Alonso, D. L. Milius, R. Car, R. K. Prudhomme and I. A. Aksay, *Chem. Mater.*, 2007, **19**, 4396–4404.
31 O. Akhavan, *Carbon*, 2010, **48**, 509–519.
32 Y. Qiu, F. Guo, R. Hurt and I. Külaots, *Carbon*, 2014, **72**, 215–223.
33 B. Zhao, P. Liu, Y. Jiang, D. Pan, H. Tao, J. Song, T. Fang and W. Xu, *J. Power Sources*, 2012, **198**, 423–427.
34 N. V. Medhekar, A. Ramasubramaniam, R. S. Ruoff and V. B. Shenoy, *ACS Nano*, 2010, **4**, 2300–2306.
35 C. Vallés, J. D. Núñez, A. M. Benito and W. K. Maser, *Carbon*, 2012, **50**, 835–844.
36 X. Wang, R. Wang, Z. Zhao, S. Bi and Z. Niu, *Energy Storage Mater.*, 2019, **23**, 269–276.
37 X. Chen, W. Li, D. Luo, M. Huang, X. Wu, Y. Huang, S. H. Lee, X. Chen and R. S. Ruoff, *ACS Nano*, 2017, **11**, 665–674.
38 W. S. Hummers and R. E. Offeman, *J. Am. Chem. Soc.*, 1958, **80**, 1339.
39 L. Feng, K. Wang, X. Zhang, X. Sun, C. Li, X. Ge and Y. Ma, *Adv. Funct. Mater.*, 2018, **28**, 1–9.
40 G. Wu, P. Tan, X. Wu, L. Peng, H. Cheng, C.-F. Wang, W. Chen, Z. Yu and S. Chen, *Adv. Funct. Mater.*, 2017, **27**, 1–11.
41 Y. Shao, M. F. El-Kady, J. Sun, Y. Li, Q. Zhang, M. Zhu, H. Wang, B. Dunn and R. B. Kaner, *Chem. Rev.*, 2018, **118**, 9233–9280.
42 X. Yang, C. Cheng, Y. Wang, L. Qiu and D. Li, *Science*, 2013, **341**, 534–537.
43 Y. Bu, T. Sun, Y. Cai, L. Du, O. Zhuo, L. Yang, Q. Wu, X. Wang and Z. Hu, *Adv. Mater.*, 2017, **29**, 1–7.
44 Y. Wang, S. Li, H. Yang and J. Luo, *RSC Adv.*, 2020, **10**, 15328–15345.

45 G. Liu, W. Jin and N. Xu, *Chem. Soc. Rev.*, 2015, **44**, 5016–5030.
46 L. Stobinski, B. Lesiak, A. Malolepszy, M. Mazurkiewicz, B. Mierzwa, J. Zemek, P. Jiricek and I. Bieloshapka, *J. Electron Spectrosc. Relat. Phenom.*, 2014, **195**, 145–154.
47 H. Saleem, M. Haneef and H. Y. Abbasi, *Mater. Chem. Phys.*, 2018, **204**, 1–7.
48 J. Li, J. Tang, J. Yuan, K. Zhang, Q. Shao, Y. Sun and L.-C. Qin, *Electrochim. Acta*, 2016, **197**, 84–91.
49 Q. Shao, J. Tang, Y. Lin, J. Li, F. Qin, J. Yuan and L.-C. Qin, *J. Power Sources*, 2015, **278**, 751–759.
50 Y. Bin Tan and J.-M. Lee, *J. Mater. Chem. A*, 2013, **1**, 14814–14843.
51 J. H. Park, O. O. Park, K. H. Shin, C. S. Jin and J. H. Kim, *Electrochem. Solid-State Lett.*, 2002, **5**, 3–7.
52 S. Dai, Z. Liu, B. Zhao, J. Zeng, H. Hu, Q. Zhang, D. Chen, C. Qu, D. Dang and M. Liu, *J. Power Sources*, 2018, **387**, 43–48.
53 V. Sedlakova, J. Sikula, J. Majzner, P. Sedlak, T. Kuparowitz, B. Buergler and P. Vasina, *J. Power Sources*, 2015, **286**, 58–65.
54 B. Song, J. Zhao, M. Wang, J. Mullavey, Y. Zhu, Z. Geng, D. Chen, Y. Ding, K. Moon, M. Liu and C.-P. Wong, *Nano Energy*, 2017, **31**, 183–193.
55 D. Wang, S. Liu, L. Jiao and G. Fang, *Electrochim. Acta*, 2017, **252**, 109–118.
56 P. Xu, Q. Gao, L. Ma, Z. Li, H. Zhang, H. Xiao, X. Liang, T. Zhang, X. Tian and C. Liu, *Carbon*, 2019, **149**, 452–461.
57 Y. Yan, N. Cui, F. Liu, X. F. Hao, Y.-H. Li, Y.-B. Zhang, Z.-Z. Pan, N. Wu and C. Hao, *J. Alloys Compd.*, 2019, **776**, 22–30.
58 Y. Zhou, J. Ren, L. Xia, Q. Zheng, J. Liao, E. Long, F. Xie, C. Xu and D. Lin, *Electrochim. Acta*, 2018, **284**, 336–345.
59 Z. Li, S. Gadipelli, Y. Yang, G. He, J. Guo, J. Li, Y. Lu, C. A. Howard, D. J. L. Brett, I. P. Parkin, F. Li and Z. Guo, *Energy Storage Mater.*, 2019, **17**, 12–21.
60 J. Zhang, J. Jiang, H. Li and X. S. Zhao, *Energy Environ. Sci.*, 2011, **4**, 4009–4015.
61 Y. Yan, N. Cui, F. Liu, X.-F. Hao, Y.-H. Li, Y.-B. Zhang, Z.-Z. Pan, N. Wu and C. Hao, *J. Alloys Compd.*, 2019, **776**, 22–30.
62 X. Wang, C. Lu, H. Peng, X. Zhang, Z. Wang and G. Wang, *J. Power Sources*, 2016, **324**, 188–198.
63 W. Yang, W. Yang, A. Song, L. Gao, L. Su and G. Shao, *J. Power Sources*, 2017, **359**, 556–567.
64 L. Lai, H. Yang, L. Wang, B. K. Teh, J. Zhong, H. Chou, L. Chen, W. Chen, Z. Shen, R. S. Ruoff and J. Lin, *ACS Nano*, 2012, **6**, 5941–5951.
65 Z. Lei, N. Christov, L. L. Zhang and X. S. Zhao, *J. Mater. Chem.*, 2011, **21**, 2274–2281.
66 Z. Li, S. Gadipelli, H. Li, C. A. Howard, D. J. L. Brett, P. R. Shearing, Z. Guo, I. P. Parkin and F. Li, *Nat. Energy*, 2020, **5**, 160–168.
67 H. Li, Y. Tao, X. Zheng, J. Luo, F. Kang, H.-M. Cheng and Q.-H. Yang, *Energy Environ. Sci.*, 2016, **9**, 3135–3142.
68 C. Zhong, Y. Deng, W. Hu, J. Qiao, L. Zhang and J. Zhang, *Chem. Soc. Rev.*, 2015, **44**, 7484–7539.
69 Z. She, D. Ghosh and M. A. Pope, *ACS Nano*, 2017, **11**, 10077–10087.
70 C. Liu, X. Yan, F. Hu, G. Gao, G. Wu and X. Yang, *Adv. Mater.*, 2018, **30**, 1–14.
71 Y. Zhang, X. Wang, F. Luo, Y. Tan, L. Zeng, B. Fang and A. Liu, *Appl. Catal., B*, 2019, **256**, 117852.
72 S. Yu, S. Song, R. Li and B. Fang, *Nanoscale*, 2020, **12**, 19536–19556.
73 L. Lu, B. Wang, D. Wu, S. Zou and B. Fang, *Nanoscale*, 2021, **13**, 3709–3722.
74 B. Fang, L. Daniel, A. Bonakdarpour, R. Govindarajan, J. Sharman and D. P. Wilkinson, *Small*, 2021, **17**, 2102288.